Super Klein tunneling in phononic Lieb lattices

Hao Wu,[1] Hailong He,[1,*] Ze Dong,[1] Liping Ye,[1] Weiyin Deng,[1,†] Manzhu Ke,[1] and Zhengyou Liu[1,2,‡]

[1] *Key Laboratory of Artificial Micro- and Nano-structures of Ministry of Education and School of Physics and Technology, Wuhan University, Wuhan 430072, China*

[2] *Institute for Advanced Studies, Wuhan University, Wuhan 430072, China*

(Received 13 December 2023; revised 23 February 2024; accepted 26 February 2024; published 14 March 2024)

Super Klein tunneling is one of the intriguing phenomena found in spin-1 systems and has aroused many research interests due to its extraordinary transport properties. Compared with the traditional Klein tunneling occurring under normal incidence, super Klein tunneling releases the restriction to omnidirectional total transmission around the center of the energy or frequency barrier. Here, we observe super Klein tunneling in a heterojunction of a phononic Lieb lattice, where a single pseudospin-1 Dirac cone is located at the corner of the square Brillouin zone and consists of two linear crossed bands accompanied by an extra flat band. Airborne sound experiments evidence the near-perfect transmissions around the center of the frequency barrier for a wide range of incident angles. Our macroscopic acoustic system with a pseudospin-1 Dirac cone provides an ideal platform to explore the physics and applications related to super Klein tunneling.

DOI: 10.1103/PhysRevApplied.21.034026

I. INTRODUCTION

Relativistic massless Dirac particles can easily pass through potential barriers regardless of their height and width upon normal incidence with a unity transmission [1]. This counterintuitive pure quantum phenomenon was first proposed theoretically by Oskar Klein in 1929 and is therefore called the Klein paradox [2]. Since there are huge difficulties in accelerating particles to a relativistic state and constructing a parallel barrier, direct observation of the Klein paradox in particle physics has not been reported up to now. However, the interesting phenomenon is easily observed in graphene with a honeycomb lattice that hosts the spin-1/2 Dirac quasiparticle with linear dispersion [3,4], which relies on the sublattice pseudospin conservation, and is now called Klein tunneling. This has aroused attention into exploring various total transmission phenomena of relativistic quasiparticles in solid materials [2,5–9] and classical wave systems [10–13]. Klein tunneling has been experimentally verified in phononic [11,12] and photonic [14] heterojunctions of honeycomb lattices.

An omnidirectional total transmission is known as super Klein tunneling (SKT), in which relativistic particles with energies of half the potential barrier can perfectly tunnel through the barrier irrespective of their incident angle [13,15–17]. This phenomenon has been found to appear in systems possessing the pseudospin-1 Dirac quasiparticle [18]. Extraordinary properties arise from the pseudospin-1 Dirac cone that exhibits a linear crossing accompanied by an additional flat band [19]. This feature enriches the transport behaviors even if the flat band does not contribute to transport, such as super collimation [13], antilocalization [20,21], super Andreev reflection [22,23], and topological charge pumping [24]. Such a pseudospin-1 Dirac cone is found to exist in dice [19], square [23], $\alpha - T_3$ [25,26], breathing [27], and Lieb [28] lattices. Very recently, SKT has been experimentally observed in phononic crystals with a triangular lattice, in which a flat band is tuned to intersect the pseudospin-1/2 Dirac cones to form a pair of pseudospin-1 Dirac cones at the hexagonal Brillouin zone corners (points K and K'), due to the resonance of Willis scatterers [29]. This naturally prompts a question about whether SKT could be observed intuitively in a cleaner system with a single pseudospin-1 Dirac cone.

In this work, we report the observation of acoustic SKT in a phononic heterojunction consisting of two types of phononic Lieb lattices (PLLs) with different pseudospin-1 Dirac frequencies. The PLL exhibits a single pseudospin-1 Dirac cone at the M point of the square Brillouin zone, which allows a convincing result without considering intervalley scattering. The scalability and controllability of the artificial structures allow us to further understand the intricate physics of pseudospin-1 quasiparticles [30–33]. We first measure perfect Klein tunneling over the

*hehailong@whu.edu.cn
†dengwy@whu.edu.cn
‡zyliu@whu.edu.cn

frequency range within the pseudospin-1 Dirac frequency barrier under normal incidence and then demonstrate the omnidirectional near-perfect transmission around the center frequency in the phononic heterojunction. The direct observation of acoustic SKT may have great significance in searching for relativistic particles and provide a new avenue in surface wave devices for signal processing and lossless communication.

II. RESULTS AND DISCUSSIONS

A. Model for acoustic super Klein tunneling

For experimental observation of acoustic SKT, we create a frequency barrier by sandwiching two types of PLLs with identical lattice constants but different geometric parameters. In classical physics, a particle encountering a high barrier is completely prohibited when its energy is lower than the height of the barrier. The amplitude of the nonrelativistic particle will have an exponentially decaying part in the barrier. Massless Dirac particles passing vertically through the barrier will exhibit perfect transmission because of their conservation of pseudospins. Some theoretical works have also found that omnidirectional perfect transmission can be achieved in pseudospin-1 systems [3,15,16,19,20,34,35]. In such Lieb lattices, the effective Hamiltonian around the pseudospin-1 Dirac cone can be described by [14]

$$H_0 = v_0 \begin{pmatrix} 0 & q_x & 0 \\ q_x & 0 & q_y \\ 0 & q_y & 0 \end{pmatrix} = v_0 \mathbf{S} \cdot \mathbf{q},$$

where v_0 is a quantity related to the group velocity, $\mathbf{q} = (q_x, q_y)$ is the momentum around the pseudospin-1 Dirac cone located at M in the Brillouin zone, and $\mathbf{S} = (S_x, S_y)$ is the vector of the pseudospin-1 matrix denoting the sublattice pseudospin. In Fig. 1(a), we show the schematic diagram of the frequency barrier of the pseudospin-1 quasiparticles. The difference between the pseudospin-1 Dirac frequencies forms a *n*-*p*-*n*-like step barrier. The green horizontal plane represents the operating frequency (energy for massless relativistic particles) within the barrier. The horizontal plane cuts out the equifrequency contours that can be used to analyze the transport behavior of the quasiparticles, as shown in Fig. 1(b), where the arrows represent the

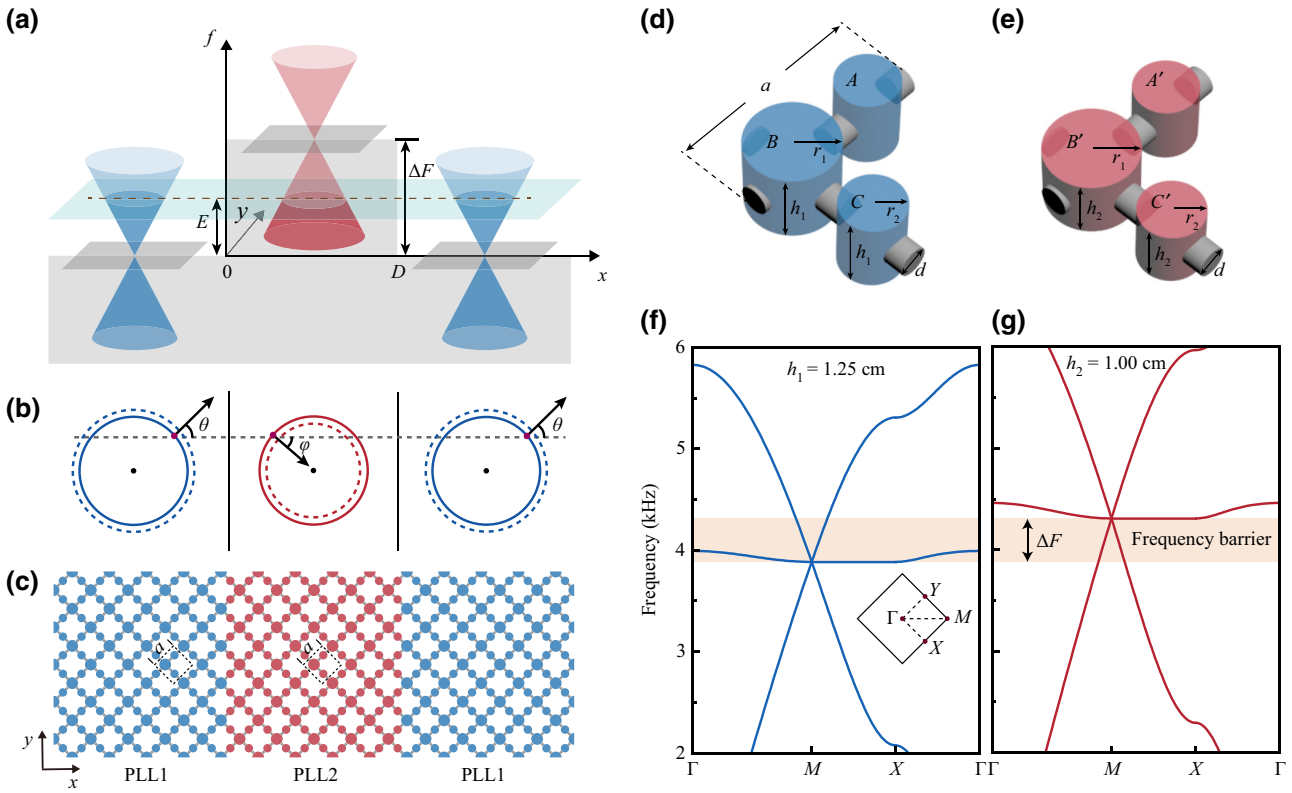

FIG. 1. SKT of acoustic pseudospin-1 Dirac quasiparticles. (a) Schematic of the frequency barrier of the Dirac-like cone with a width of D and height ΔF. (b) Equifrequency contour analysis for a frequency within the frequency barrier. Solid and dashed curves represent the equifrequency contours and the slightly larger ones, respectively. Arrows indicate the directions of group velocity corresponding to PLL1 and PLL2. (c) A phononic heterojunction composed of two types of PLLs with different geometric parameters. (d),(e) Enlarged views of the unit cell depicted by the black dashed boxes in (c). (f),(g) Bulk band structures of PLL1 and PLL2, with $h_1 = 1.25$ cm and $h_1 = 1.00$ cm, respectively. The inset of (f) shows the first Brillouin zone.

directions of the group velocity. We can conclude that there are two negative refraction effects at the interfaces [36,37]. The pseudospin-1 quasiparticles in our systems are mimicked by acoustic threefold degeneracy from the PLL, in which the pseudospin-1 Dirac cone is formed by an additional flat band crossing a linear dispersion at the M point of the square Brillouin zone. The heterojunction barrier is constructed by the two PLLs (PLL1 and PLL2), as shown in Fig. 1(c). The width of the barriers and interface details are consistent with actual samples, but the overall size is not the same.

The unit cells of PLL1 [Fig. 1(d)] and PLL2 [Fig. 1(e)] are composed of three cylindrical cavities, labeled A and A', B and B', and C and C', respectively, which are coupled by two orthogonal cylindrical tubes with identical diameters of $d = 0.46$ cm. The unit cells have the same lattice constant $a = 3.00$ cm. Both have one big cavity B and B′ with $r_1 = 0.69$ cm and two identical small cavities A and A′, and C and C′ with $r_2 = 0.48$ cm, which can be regarded as lattice sites in general. The only difference between PLL1 and PLL2 is the height of cavities: $h_1 = 1.25$ cm for all three cavities in PLL1 and $h_2 = 1.00$ cm in PLL2. By adjusting the height of cavities, we can shift the frequency positions of the pseudospin-1 Dirac point. The corresponding band structures are shown in Figs. 1(f) and 1(g) [Appendix A]. The two pseudospin-1 Dirac points with $f_1 = 3.88$ kHz and $f_2 = 4.31$ kHz form a frequency barrier $\Delta F = 0.43$ kHz. It can be seen that the conical dispersions around the pseudospin-1 Dirac points are linearly touched by a flat band, and match well with the massless low-energy effective Hamiltonian.

B. Observation of traditional Klein tunneling in PLLs

For an experimental observation, a heterojunction of the PLL sample is produced by 3D photosensitive resin printing. The experimental setup is shown in Fig. 2(a). The frequency barrier (PLL2) is outlined by the dashed box and is $5\sqrt{2}a \times 40\sqrt{2}a$ in the x and y directions. Two PLL1s before and after the barrier have a mirror symmetry about

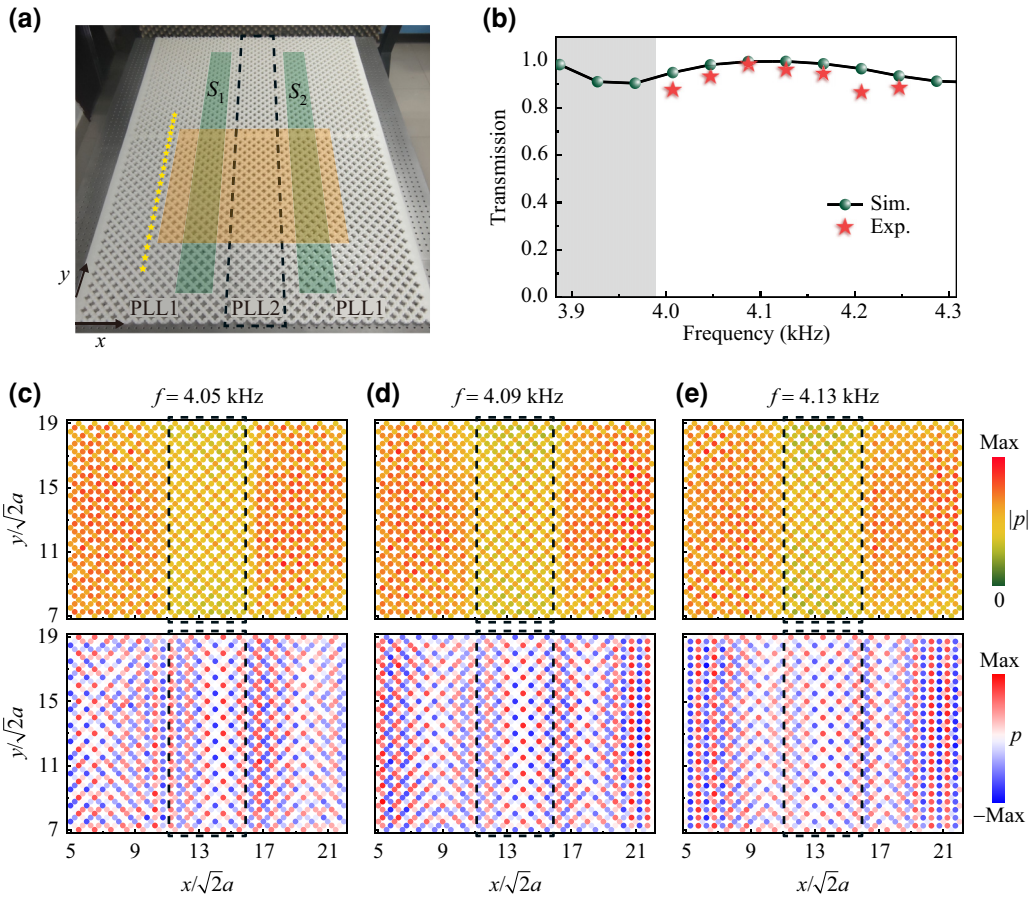

FIG. 2. Experimental setup and observation of traditional Klein tunneling. (a) Photo of the phononic heterojunction. The green rectangular ribbons, orange square area, and black dashed box denote the measured areas of the transmission, scanning region of the field, and frequency barrier region, respectively. The yellow stars indicate the positions of the point sound source. (b) Measured transmission (red stars) as a function of the frequency within the barrier compared with the simulated results (green balls). (c)–(e) Measured field distributions for three frequencies all within the frequency barrier. The top and bottom panels show the normalized amplitude and pressure fields, respectively.

the center line of the PLL2. The size of each PLL1 is $13\sqrt{2}a \times 40\sqrt{2}a$ in the x and y directions. To avoid reflection from the upper and lower boundaries, the source array (yellow stars) is positioned at the bottom middle half of the sample. The point sources are placed in cavity B of each cell for better excitations. By gradually varying the initial phase of each point source, we can obtain a plane wave with incident angle θ in the left PLL1. We first measure the frequency-dependent transmission under normal incidence. The point sources launch wide-frequency sound signals with the same amplitude and phase, resulting in a plane wave being excited to impact the barrier PLL2 under normal incidence. In a PLL, the energy of sound waves can be characterized by energy flux density $I = |p|^2/\rho_{\text{eff}} v_g = (1/2)A^2/Z_{\text{eff}}$, where p is sound pressure, A amplitude, ρ_{eff} effective mass density, v_g group velocity, and Z_{eff} effective acoustic impedance. Because the regions before and after the barrier are both PLL1 with the same Z_{eff}, the transmission can be obtained by

$$T = \frac{\iint_{S_2} A^2 ds}{\iint_{S_1} A^2 ds},$$

where S_1 and S_2 are the measured regions before and after the potential barrier denoted by the dashed box, with the same area. The integration region almost covers the y direction to collect all the energy passing through the barrier. In this type of PLL with a cavity-tube structure, the dissipative effect of the resin material on sound waves is inevitable. To reduce the influence of dissipation on experimental observation, we extract the dissipation coefficients to compensate the amplitude fields for different frequencies and incident angles in PLL1 and PLL2, respectively [Appendix B].

Figure 2(b) exhibits the frequency-dependent transmission under normal incidence. The maximum and minimum of the horizontal axis are the frequencies of two pseudospin-1 Dirac points. The measured results for the frequency of the gray area are not given because this area overlaps the frequency range of the near-flat band of PLL1. It can be seen that both the simulated and measured transmission spectra have overall high transmissions and good consistency, indicating the applicability of the experimental approach. The negligible differences between them may be caused by the collection of unexpected diffusion states described above, the finite size of the sample, and defects in manufacturing and splicing the sample. To further visualize the Klein tunneling, we measure the normalized amplitude and pressure field distributions, as shown in Figs. 2(c)–2(e). The measured region is depicted by the orange rectangle in Fig. 2(a). From the upper panels of Figs. 2(c)–2(e), we can see that the consistency of amplitude intensity on both sides of the barrier again verifies the perfect transmission. The difference in amplitude inside and outside the barrier is due to the mismatch of the effective acoustic impedance. From the bottom panels of Figs. 2(c)–2(e), we can obtain an effective wavelength of about 11 unit cells in the x direction, which is twice the distance between the light and dark stripes in the pressure fields. This is much longer than the wavelength in air. These wave fronts also indicate the horizontal propagation directions of the acoustic wave in the whole heterojunction.

C. Observation of super Klein tunneling in PLLs

We measure the transmission of the phononic heterojunction as a function of incident angle at the center frequency of 4.09 kHz, where the equifrequency contours of this frequency for PLL1 and PLL2 are identical.

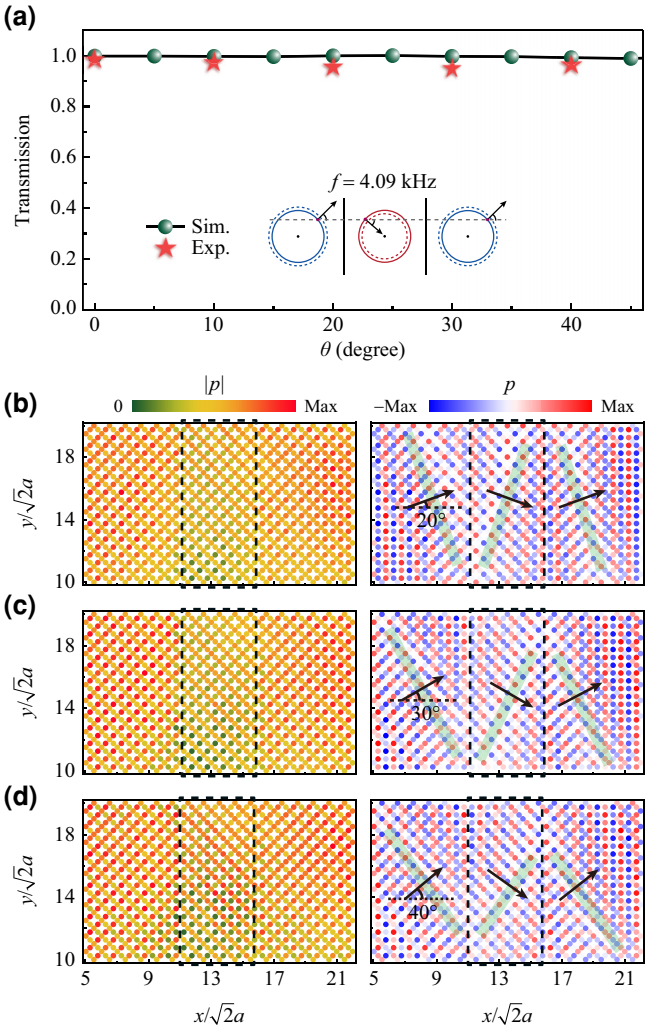

FIG. 3. Observation of SKT at the center frequency of 4.09 kHz. (a) Measured and simulated angle-dependent transmission spectra. (b)–(d) Normalized amplitude field $|p|$ (left panel) and pressure field p (right panel) for different incident angles. In the right panels, the light green strips and black arrows mark the effective wave front and the directions of group velocity in the PLL, respectively.

Figure 3(a) gives the angle-dependent transmission spectra. Owing to the limitation of the sample size, we only measure the transmission where the incident angle is less than 40°. Because the heterojunction has a mirror symmetry, only the transmissions with a positive incident angle are given. The measured transmissions (red stars) reach up to 0.985, 0.973, 0.955, 0.949, and 0.963 for $\theta = 0°$, 10°, 20°, 30°, and 40°, respectively, which are in good agreement with the near-unity transmission in simulation (green balls). The measured transmissions here are compensated by their corresponding dissipation coefficients. Such near-unity transmissions independent of the width and height of the potential barrier are shown in Figs. 6(a) and 6(b) [Appendices C and D]. Furthermore, we also give the normalized amplitude and pressure fields for $\theta = 20°$, 30°, and 40°, as shown in Figs. 3(b)–3(d). The magnitudes of amplitude are invariant overall before and after the barrier, indicating the near-perfect transmission at these incident angles. The sound pressure fields are shown in the right-hand panels. Similar to the normal incidence, several wide stripes highlighted in green indicate the wave front and the black arrows denote the directions of group velocity. One can see that negative refractions occur at both the PLL1-PLL2 and PLL2-PLL1 interfaces, verifying the previous predictions from equifrequency contour analysis.

To further characterize the tunneling properties, we measure the behaviors of angle-dependent transmission near the center frequency. The measured and simulated transmission results at the frequency 4.05 kHz are shown in Fig. 4(a). The measured transmissions (red stars) reach up to 0.931, 0.935, 0.925, 0.933, and 0.894 for $\theta = 0°$, 10°, 20°, 30°, and 40°, respectively, which are slightly lower than the simulated results (green balls). The measured transmissions here are also compensated by their corresponding dissipation coefficients. It can be seen that the transmission spectrum reaches a maximum of 1 at $\theta = 0$, which corresponds to traditional Klein tunneling. Above 30° incidence, the transmission slowly decreases to reach the value 0.810 at an incident angle of 45°. For 4.13 kHz, when incident angle θ in PLL1 exceeds 30°, the refraction angle φ would be much larger than 30°, which makes it impossible to measure the attenuation in the barrier due to the finite size of the sample, thus the maximum of the incident angle in the measured transmission is 30°, as shown in Fig. 4(c). In contrast with transmission at 4.05 kHz, the transmission at 4.13 kHz decreases rapidly for large incident angles. As shown in Figs. 3(b) and 3(d), the wide-angle perfect transmission can be visualized by the amplitude and pressure fields. In Figs. 4(b) and 4(d), we display the field distributions for 4.05 and 4.13 kHz. Overall, the magnitudes of amplitude are almost unchanged before and after the barrier. Several wide stripes highlighted in green indicate the wave front and the black arrows denote the directions of group

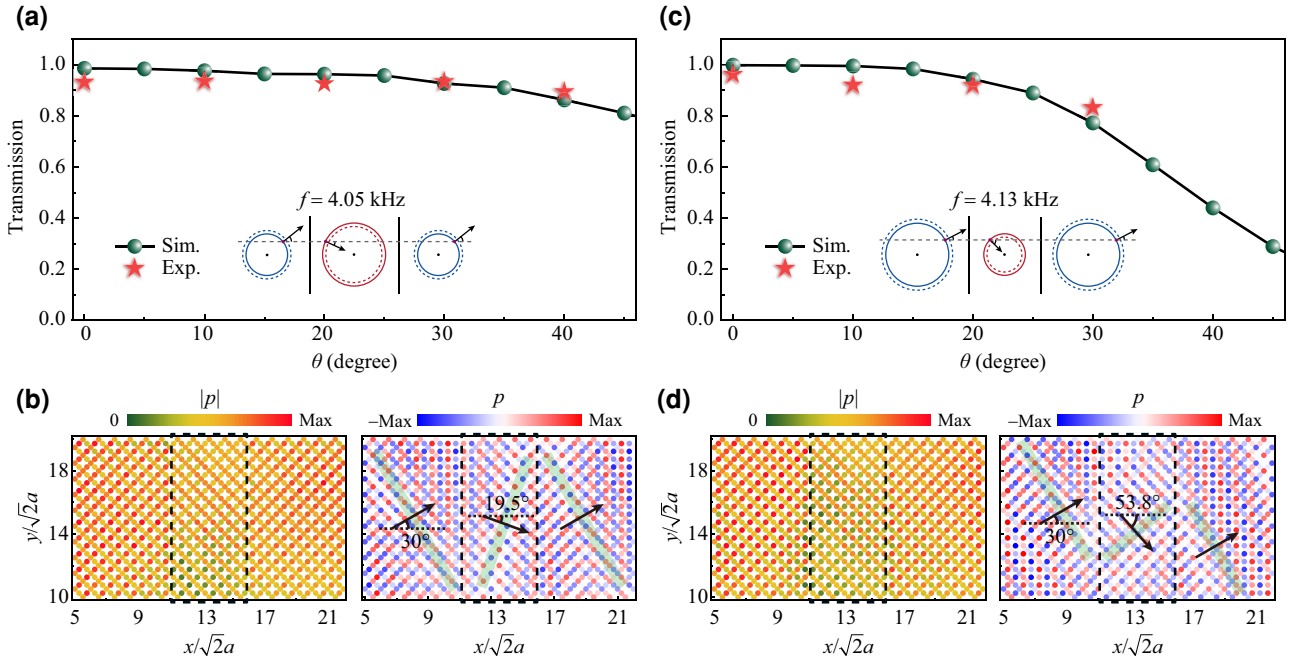

FIG. 4. Observation of wide-angle near-perfect transmissions around the center frequency. (a) Measured and simulated transmissions as a function of the incident angle at 4.05 kHz. (b) Normalized amplitude field $|p|$ (left panel) and pressure field p (right panel) under the incident angle of 30°. In the right panel, the light green strips and black arrows mark the effective wave front and the directions of group velocity, respectively. (c),(d) The same as (a),(b) but at 4.13 kHz. The inset of (a),(c) label the positions of the operating frequencies within the barrier.

velocity. The measured refraction angles φ are approximately equal to 19.5° and 53.8° for 4.05 and 4.13 kHz, respectively, which agree well with the predictions from equifrequency contour analysis.

III. CONCLUSIONS

In summary, we construct a PLL heterojunction and unambiguously observe SKT, in which the PLL hosts only a single pseudospin-1 Dirac cone in the square Brillouin zone corner. By varying the heights of the resonant cavities, we can shift the frequencies of the pseudospin-1 Dirac cone to assemble the phononic heterojunction with a frequency barrier. As a signature feature of SKT, omnidirectional total transmissions at the center of the frequency barrier are verified in experiments, which are in good agreement with the simulations. When the operating frequency is slightly away from the center, near-perfect transmissions are still observed at a wide range of incident angles. Our work expands the conditions for unobstructed energy transmission in sound waves, which provides ideas for research into robust transmission and may have potential significance for acoustic-integrated devices.

ACKNOWLEDGMENTS

This work is supported by the National Key R&D Program of China (Grants No. 2022YFA1404900, No. 2022YFA1404500) and the National Natural Science Foundation of China (Grants No. 12074128, No. 12104347, No. 12222405, No. 12374409, No. 12374419).

APPENDIX A: NUMERICAL SIMULATIONS

Throughout this work, all the simulations are performed using commercial finite-element software COMSOL Multiphysics, and the mass density and sound speed of air are set as 1.29 kg/m^3 and 341 m/s, respectively. Owing to the huge acoustic impedance mismatch between photosensitive resin and air, the 3D-printed material is regarded as a rigid boundary in simulations. The bulk band structures in Figs. 1(f) and 1(g) are calculated by applying the Bloch boundary conditions in both the x and y directions. A semi-infinite heterojunction with Bloch periodic boundary conditions in the y direction but with an absorbing boundary in the x direction is used to calculate the transmissions. A monopole point source is used to stimulate the Bloch mode in PLL1. Different incident directions are achieved by varying the Bloch wave vectors k_y. The simulated transmissions in Figs. 2(b), 3(a), 4(a), and 4(c) are calculated by collecting the energy in the same sized regions before and after the frequency barrier.

APPENDIX B: EXPERIMENTAL MEASUREMENTS

Note that the size of the sample in the x and y directions is large enough that there is no need to consider reflections in the experiment due to the natural attenuation. The natural attenuation of acoustic intensity can be expressed as $I(x) = I_0 \exp(-mx)$, where I_0 is the intensity at the initial position, which is proportional to A^2, and m is the attenuation coefficient to be measured. We measure

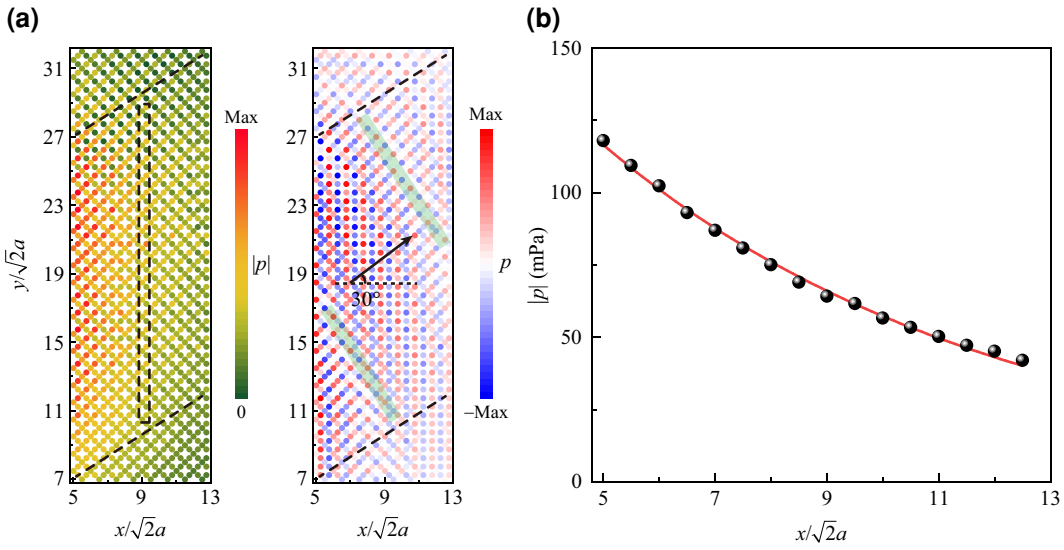

FIG. 5. Measurement of attenuation coefficient m. (a) Measured amplitude (left panel) and pressure (right panel) fields in a uniform PLL1. The oblique dashed lines outline the region of integration of acoustic fields. The square of the amplitude within the dashed box is used for the calculation of the attenuation coefficient. (b) Fitting of measured values in (a).

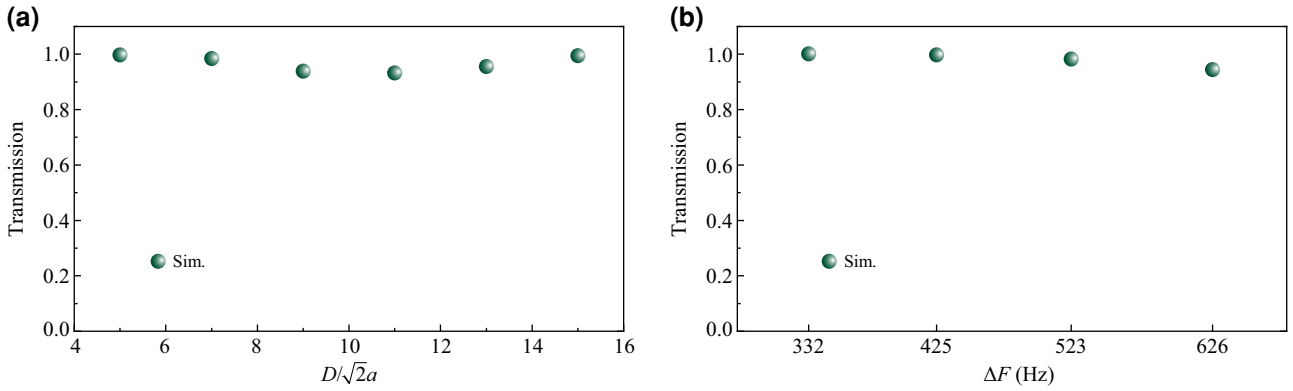

FIG. 6. SKT under different widths and heights of the barriers for $\theta = 30°$. (a) Simulated transmission T as a function of width D at $f = 4.09$ kHz. (b) Simulated transmission as a function of heights ΔF for width $D = 5\sqrt{2}a$.

the coefficient $m^{\theta}_{1(2)}$ for different incident angles θ and frequencies in a uniform PLL1 or PLL2. The source array is positioned at the left side of the sample PLL1 or PLL2. A multiaudio channel sound card (Antelope Orion32+ Gen3) is utilized to generate discrete acoustic signals. By gradually varying the initial phase of each point source, we can obtain a plane wave with incident angle θ in the left PLL1. A series of subwavelength speakers (diameter ∼4.0 mm) are used as point sound sources. Two identical acoustic detectors (B&K Type 4187 1/4-in. microphone) are employed for sound recording: one is fixed near the sound source to collect the reference signals; the other is moved cavity by cavity to capture the field distributions. A multianalyzer system (B&K Type 3560B) is used to analyze signals. In Fig. 5, we pick $\theta = 30°$ and $f = 4.09$ kHz in PLL1 as an example to illustrate the measurement process of the attenuation coefficient $m_1^{30°}$. The measured amplitude and pressure fields are shown in Fig. 5(a). The sound waves mainly travel between the oblique dashed lines with $\theta = 30°$. The dissipative spectrum of the acoustic field is characterized by integrating the energy in the rectangular dashed box. Then, the attenuation coefficient $m_1^{30°}$ can be obtained by fitting the dissipative spectrum exhibited in Fig. 5(b). The measured field distributions can be compensated using their corresponding m.

APPENDIX C: TRANSMISSIONS THROUGH FREQUENCY BARRIERS WITH DIFFERENT WIDTHS AND HEIGHTS

For further discussion, we calculate the transmission with different widths and heights of the barrier under an incidence of $\theta = 30°$, as shown in Figs. 6(a) and 6(b). In Fig. 6(a), we give the transmission as a function of the width of the barriers at the center frequency $f = 4.09$ kHz for the heterojunction composed of PLL1 and PLL2. In Fig. 6(b), we give the transmission as a function of the heights of the barriers for four heterojunctions. Both results display a near-unity transmission, which verifies the stability of the SKT.

APPENDIX D: SIMULATED TRANSMISSIONS FOR THE WIDER RANGE OF INCIDENT ANGLE

In Figs. 3 and 4, we have given the transmission at a certain range of incident angles at different frequencies. If we were not limited to comparing with experimental conditions, we could give the ideal simulated transmissions for a wider range of angles of incidence, with a longer PLL1 and wider integration area, as shown in Fig. 7. The results are consistent with the conclusions in the text, where the SKT is still obvious at the center frequency. At angles of incidence above 80°, ideal simulation is also hard to achieve because of the reflection between the PLL1 and the drain areas on both sides.

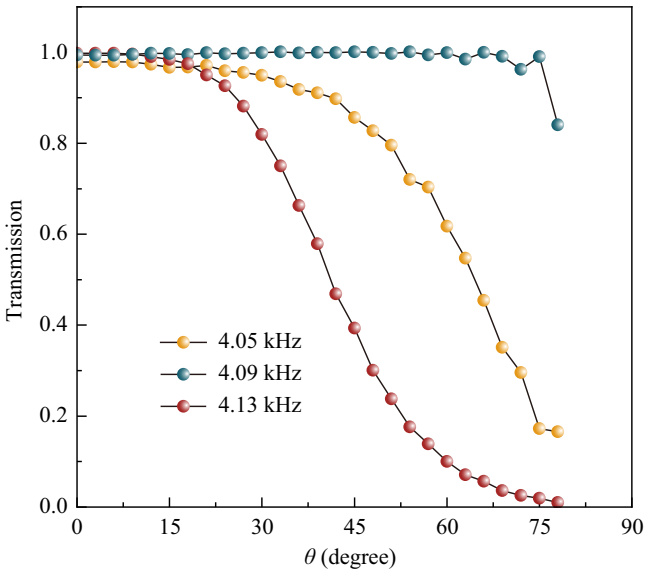

FIG. 7. Simulated transmission as functions of incident angle at $f = 4.05$, 4.09, and 4.13 kHz.

[1] O. Klein, Die Reflexion von Elektronen an einem Potentialsprung nach der relativistischen Dynamik von Dirac, Z. Phys. **53**, 157 (1929).

[2] M. I. Katsnelson, K. S. Novoselov, and A. K. Geim, Chiral tunnelling and the Klein paradox in graphene, Nat. Phys. **2**, 620 (2006).

[3] P. E. Allain and J. N. Fuchs, Klein tunneling in graphene: Optics with massless electrons, Eur. Phys. J. B **83**, 301 (2011).

[4] A. H. Castro Neto, F. Guinea, N. M. R. Peres, K. S. Novoselov, and A. K. Geim, The electronic properties of graphene, Rev. Mod. Phys. **81**, 109 (2009).

[5] N. Stander, B. Huard, and D. Goldhaber-Gordon, Evidence for Klein tunneling in graphene *p-n* junctions, Phys. Rev. Lett. **102**, 026807 (2009).

[6] S. Chen, Z. Han, M. M. Elahi, K. M. M. Habib, L. Wang, B. Wen, Y. Gao, T. Taniguchi, K. Watanabe, J. Hone, A. W. Ghosh, and C. R. Dean, Electron optics with p-n junctions in ballistic graphene, Science **353**, 1522 (2016).

[7] T. Ozawa, A. Amo, J. Bloch, and I. Carusotto, Klein tunneling in driven-dissipative photonic graphene, Phys. Rev. A **96**, 013813 (2017).

[8] T. Tudorovskiy, K. J. A. Reijnders, and M. I. Katsnelson, Chiral tunneling in single-layer and bilayer graphene, Phys. Scr. **T146**, 014010 (2012).

[9] T. R. Robinson, On Klein tunneling in graphene, Am. J. Phys. **80**, 141 (2012).

[10] X. Jiang, C. Z. Shi, Z. L. Li, S. Q. Wang, Y. Wang, S. Yang, S. G. Louie, and X. Zhang, Direct observation of Klein tunneling in phononic crystals, Science **370**, 1447 (2020).

[11] L. Sirota, Klein-like tunneling of sound via negative index metamaterials, Phys. Rev. Appl. **18**, 014057 (2022).

[12] N. Gao, J. Wang, and W. Chen, Klein tunneling for Lamb waves in elastic phononic crystal plates, Appl. Phys. Lett. **121**, 102201 (2022).

[13] A. Fang, Z. Q. Zhang, S. G. Louie, and C. T. Chan, Klein tunneling and supercollimation of pseudospin-1 electromagnetic waves, Phys. Rev. B **93**, 035422 (2016).

[14] Z. Zhang, Y. Feng, F. Li, S. Koniakhin, C. Li, F. Liu, Y. Zhang, M. Xiao, G. Malpuech, and D. Solnyshkov, Angular-dependent Klein tunneling in photonic graphene, Phys. Rev. Lett. **129**, 233901 (2022).

[15] R. Shen, L. B. Shao, B. Wang, and D. Y. Xing, Single Dirac cone with a flat band touching on line-centered-square optical lattices, Phys. Rev. B **81**, 041410 (2010).

[16] A. M. Korol, A. I. Sokolenko, and O. Shevchenko, Chiral tunneling through the single barrier structure based on the α-T_3 model, Low Temp. Phys. **47**, 300 (2021).

[17] Y. Xu and G. Jin, Omnidirectional transmission and reflection of pseudospin-1 Dirac fermions in a Lieb superlattice, Phys. Lett. A **378**, 3554 (2014).

[18] B. Bradlyn, J. Cano, Z. Wang, M. G. Vergniory, C. Felser, R. J. Cava, and B. A. Bernevig, Beyond Dirac and Weyl fermions: Unconventional quasiparticles in conventional crystals, Science **353**, aaf5037 (2016).

[19] D. F. Urban, D. Bercioux, M. Wimmer, and W. Häusler, Barrier transmission of Dirac-like pseudospin-one particles, Phys. Rev. B **84**, 115136 (2011).

[20] A. Fang, Z. Q. Zhang, S. G. Louie, and C. T. Chan, Nonuniversal critical behavior in disordered pseudospin-1 systems, Phys. Rev. B **99**, 014209 (2019).

[21] S. Kim and K. Kim, Anderson localization of two-dimensional massless pseudospin-1 Dirac particles in a correlated random one-dimensional scalar potential, Phys. Rev. B **100**, 104201 (2019).

[22] W. Zeng and R. Shen, Andreev reflection of massive pseudospin-1 fermions, New J. Phys. **24**, 043021 (2022).

[23] X. Feng, Y. Liu, Z.-M. Yu, Z. Ma, L. K. Ang, Y. S. Ang, and S. A. Yang, Super-Andreev reflection and longitudinal shift of pseudospin-1 fermions, Phys. Rev. B **101**, 235417 (2020).

[24] X.-H. Wang, J. J. Wang, J. Wang, and J.-F. Liu, Flat band assisted topological charge pump in the dice lattice, Phys. Rev. B **103**, 195442 (2021).

[25] D. Bercioux, D. F. Urban, H. Grabert, and W. Häusler, Massless Dirac-Weyl fermions in a T_3 optical lattice, Phys. Rev. A **80**, 063603 (2009).

[26] E. Illes and E. J. Nicol, Klein tunneling in the $\alpha-T_3$ model, Phys. Rev. B **95**, 235432 (2017).

[27] K. Essafi, L. D. C. Jaubert, and M. Udagawa, Flat bands and Dirac cones in breathing lattices, J. Phys.: Condens. Matter **29**, 315802 (2017).

[28] D. Guzmán-Silva, C. Mejía-Cortés, M. A. Bandres, M. C. Rechtsman, S. Weimann, S. Nolte, M. Segev, A. Szameit, and R. A. Vicencio, Experimental observation of bulk and edge transport in photonic Lieb lattices, New J. Phys. **16**, 063061 (2014).

[29] Y. Zhu, A. Merkel, L. Cao, Y. Zeng, S. Wan, T. Guo, Z. Su, S. Gao, H. Zeng, H. Zhang, and B. Assouar, Experimental observation of super-Klein tunneling in phononic crystals, Appl. Phys. Lett. **122**, 211701 (2023).

[30] W. Deng, X. Huang, J. Lu, F. Li, J. Ma, S. Chen, and Z. Liu, Acoustic spin-1 Weyl semimetal, Sci. China: Phys., Mech. Astron. **63**, 287032 (2020).

[31] D. Leykam, O. Bahat-Treidel, and A. S. Desyatnikov, Pseudospin and nonlinear conical diffraction in Lieb lattices, Phys. Rev. A **86**, 031805(R) (2012).

[32] S. Mukherjee, A. Spracklen, D. Choudhury, N. Goldman, P. Ohberg, E. Andersson, and R. R. Thomson, Observation of a localized flat-band state in a photonic Lieb lattice, Phys. Rev. Lett. **114**, 245504 (2015).

[33] W. Deng, X. Huang, J. Lu, V. Peri, F. Li, S. D. Huber, and Z. Liu, Acoustic spin-Chern insulator induced by synthetic spin-orbit coupling with spin conservation breaking, Nat. Commun. **11**, 3227 (2020).

[34] Y. Betancur-Ocampo, G. Cordourier-Maruri, V. Gupta, and R. de Coss, Super-Klein tunneling of massive pseudospin-one particles, Phys. Rev. B **96**, 024304 (2017).

[35] J. Wang and J.-F. Liu, Super-Klein tunneling and electron-beam collimation in the honeycomb superlattice, Phys. Rev. B **105**, 035402 (2022).

[36] C. Qiu, X. Zhang, and Z. Liu, Far-field imaging of acoustic waves by a two-dimensional sonic crystal, Phys. Rev. B **71**, 054302 (2005).

[37] H. He, C. Qiu, L. Ye, X. Cai, X. Fan, M. Ke, F. Zhang, and Z. Liu, Topological negative refraction of surface acoustic waves in a Weyl phononic crystal, Nature (London) **560**, 61 (2018).